The Astrophysical Journal, 961:247 (14pp), 2024 February 1 https://doi.org/10.3847/1538-4357/ad11e1

Evidence of Weak Circumstellar Medium Interaction in the Type II SN 2023axu

Manisha Shrestha[1], Jeniveve Pearson[1], Samuel Wyatt[2], David J. Sand[1], Griffin Hosseinzadeh[1], K. Azalee Bostroem[1,18], Jennifer E. Andrews[3], Yize Dong (董一泽)[4], Emily Hoang[4], Daryl Janzen[5], Jacob E. Jencson[6], Michael Lundquist[7], Darshana Mehta[4], Nicolás Meza Retamal[4], Stefano Valenti[4], Jillian C. Rastinejad[8], Phil Daly[1], Dallan Porter[9], Joannah Hinz[9], Skyler Self[9], Benjamin Weiner[9], G. Grant Williams[1,9], Daichi Hiramatsu[10,11], D. Andrew Howell[12,13], Curtis McCully[12,13], Estefania Padilla Gonzalez[12,13], Craig Pellegrino[12,13], Giacomo Terreran[12,13], Megan Newsome[12,13], Joseph Farah[12,13], Koichi Itagaki[14], Saurabh W. Jha[15], Lindsey Kwok[15], Nathan Smith[1], Michaela Schwab[15], Jeonghee Rho[16], and Yi Yang[17]
[1] Steward Observatory, University of Arizona, 933 North Cherry Avenue, Tucson, AZ 85721-0065, USA; mshrestha1@arizona.edu
[2] Department of Astronomy, University of Washington, 3910 15th Avenue NE, Seattle, WA 98195-0002, USA
[3] Gemini Observatory, 670 North A'ohoku Place, Hilo, HI 96720-2700, USA
[4] Department of Physics and Astronomy, University of California, Davis, 1 Shields Avenue, Davis, CA 95616-5270, USA
[5] Department of Physics & Engineering Physics, University of Saskatchewan, 116 Science Place, Saskatoon, SK S7N 5E2, Canada
[6] Department of Physics and Astronomy, The Johns Hopkins University, 3400 North Charles Street, Baltimore, MD 21218, USA
[7] W. M. Keck Observatory, 65-1120 Māmalahoa Highway, Kamuela, HI 96743-8431, USA
[8] Center for Interdisciplinary Exploration and Research in Astrophysics (CIERA) and Department of Physics and Astronomy, Northwestern University, Evanston, IL 60208, USA
[9] MMT and Steward Observatories, University of Arizona, 933 North Cherry Avenue, Tucson, AZ 85721-0065, USA
[10] Center for Astrophysics | Harvard & Smithsonian, 60 Garden Street, Cambridge, MA 02138-1516, USA
[11] The NSF AI Institute for Artificial Intelligence and Fundamental Interactions, USA
[12] Las Cumbres Observatory, 6740 Cortona Drive, Suite 102, Goleta, CA 93117-5575, USA
[13] Department of Physics, University of California, Santa Barbara, CA 93106-9530, USA
[14] Itagaki Astronomical Observatory, Yamagata 990-2492, Japan
[15] Department of Physics and Astronomy, Rutgers, The State University of New Jersey, 136 Frelinghuysen Road, Piscataway, NJ 08854-8019, USA
[16] SETI Institute, 339 Bernardo Avenue, Suite 200, Mountain View, CA 94043, USA
[17] Department of Astronomy, University of California, Berkeley, Berkeley, CA 94720-3411, USA
Received 2023 October 6; revised 2023 November 17; accepted 2023 November 30; published 2024 January 31

Abstract

We present high-cadence photometric and spectroscopic observations of SN 2023axu, a classical Type II supernova with an absolute *V*-band peak magnitude of -17.2 ± 0.1 mag. SN 2023axu was discovered by the Distance Less Than 40 Mpc (DLT40) survey within 1 day of the last nondetection in the nearby galaxy NGC 2283 at 13.7 Mpc. We modeled the early light curve using a recently updated shock cooling model that includes the effects of line blanketing and found the explosion epoch to be MJD 59971.48 ± 0.03 and the probable progenitor to be a red supergiant. The shock cooling model underpredicts the overall UV data, which point to a possible interaction with circumstellar material. This interpretation is further supported by spectral behavior. We see a ledge feature around 4600 Å in the very early spectra (+1.1 and +1.5 days after the explosion), which can be a sign of circumstellar interaction. The signs of circumstellar material are further bolstered by the presence of absorption features blueward of Hα and Hβ at day >40, which is also generally attributed to circumstellar interaction. Our analysis shows the need for high-cadence early photometric and spectroscopic data to decipher the mass-loss history of the progenitor.

Unified Astronomy Thesaurus concepts: Core-collapse supernovae (304); Type II supernovae (1731); Red supergiant stars (1375); Stellar mass loss (1613); Circumstellar matter (241)

Supporting material: data behind figure

1. Introduction

Massive stars with $M_{\rm ZAMS} > 8\ M_{\odot}$ end their lives with energetic explosions known as core-collapse supernovae (CCSNe). SNe that exhibit hydrogen in their spectra are classified as Type II[19] (SNe II) and are the most common type of CCSNe (Li et al. 2011; Smith et al. 2011). The progenitors of these explosions are red supergiant (RSG) stars, which has been confirmed by direct observations (see, e.g., Smartt 2015; Van Dyk 2017). However, there are still many open questions about SN II progenitors, including the mass-loss rate of the progenitor RSG during the last years prior to explosion (e.g., Ekström et al. 2012; Beasor et al. 2020; Massey et al. 2023).

The mass-loss rate of RSGs in the months to years prior to explosion is difficult to observe directly (Smith 2014). However, the circumstellar material (CSM) created by this mass loss can have an impact on both the light curve (Morozova et al. 2018) and spectra (Bruch et al. 2021) of SNe II at very early times. In the absence of CSM interaction, the early light-curve evolution can be modeled considering shock breakout physics and subsequent cooling (e.g., Rabinak & Waxman 2011; Sapir & Waxman 2017; Morag et al. 2023).

[18] LSSTC Catalyst Fellow.
[19] In this paper we use the term Type II to refer to both the Type IIP and IIL subtypes.

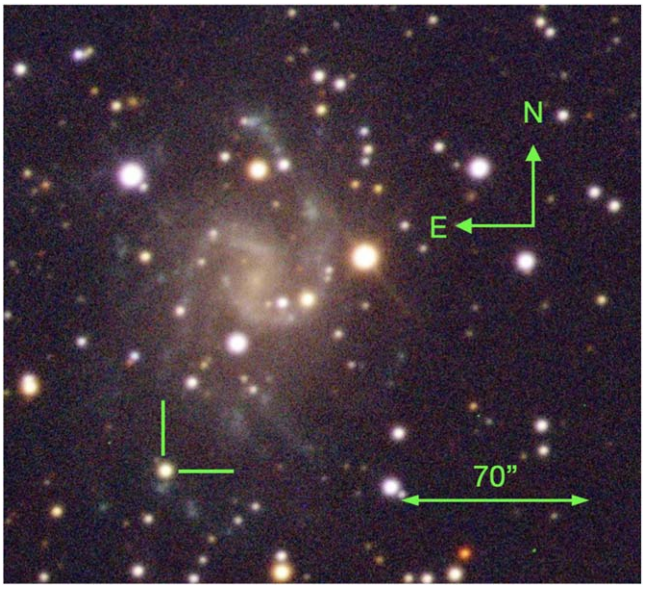

Figure 1. Composite g, r, and i image of SN 2023axu indicated by green tick marks in NGC 2283 obtained by Las Cumbres Observatory on MJD 60058.37 (+87 days after explosion).

However, when such models have been implemented, they do not match the early light-curve evolution, often with discrepancies in the light-curve rise and/or the bluest filters (e.g., Hosseinzadeh et al. 2018; Tartaglia et al. 2018; Andrews et al. 2019; Dong et al. 2021; Hosseinzadeh et al. 2022, 2023; Pearson et al. 2023). Morozova et al. (2017, 2018) found that radiation-hydrodynamical models with dense CSM fit the majority of early light curves of SNe II better than those without material around the progenitor star, pointing to the prevalence of CSM interaction. In addition to light curves, early spectra within hours to days of explosion can include clues about the CSM interaction in the form of emission lines created by the ionization of surrounding CSM by photons from shock breakout known as “flash” (e.g., Gal-Yam et al. 2014; Yaron et al. 2017; Bruch et al. 2021; Tartaglia et al. 2021; Terreran et al. 2022; Bostroem et al. 2023c; Bruch et al. 2023; Hiramatsu et al. 2023; Jacobson-Galán et al. 2023) or a broad feature (“ledge”) that could be created by CSM interaction (e.g., Soumagnac et al. 2020; Bruch et al. 2021; Hosseinzadeh et al. 2022; Bostroem et al. 2023b; Pearson et al. 2023). All these studies show the value of early observations of SNe II. The latest generation of transient surveys has been successful in gathering impressive photometric data; however, rapid spectroscopic follow-up has often been limited in terms of quantity, resolution, and signal-to-noise ratio.

In this paper, we discuss the observations and analysis of the SN II SN 2023axu. SN 2023axu was first discovered by the Distance Less Than 40 Mpc (DLT40) survey (Tartaglia et al. 2018) on 2023 January 28 (MJD 59972.11) with a discovery magnitude of 15.64 ± 0.01 in the clear filter (Sand et al. 2023), with the last nondetection on MJD 59971.08 from DLT40 (Sand et al. 2023) with a limiting magnitude of 20.04 mag. The tighter nondetection on MJD 59971.517 was obtained by K. Itagaki with a limiting unfiltered magnitude of 19 mag. The DLT40 group reported the host galaxy to be NGC 2283 as shown in Figure 1 along with SN 2023axu. The J2000 coordinates of the SN are R.A. 06:45:55.32 and decl. −18:13:53.48. The SN was classified as an SN II by Bostroem et al. (2023a) based on weak and broad hydrogen lines. The Type II classification was confirmed by the LiONS collaboration (Li et al. 2023) the following day. We made use of PYMMT (Wyatt et al. 2023) to trigger spectroscopic follow-up, which resulted in an early spectrum within a day of discovery and +1.1 days after the explosion epoch. The properties of SN 2023axu are presented in Table 1.

Table 1
Properties of SN 2023axu

Parameter	Value
R.A.	06:45:55.32 (J2000)
Decl.	−18:13:53.52 (J2000)
Last nondetection	MJD 59971.52
First detection	MJD 59972.12
Explosion epoch[a]	MJD 59971.48 ± 0.03
Redshift z	0.002805
Distance	13.68 ± 2.05 Mpc
Distance modulus (μ)	30.68 ± 0.32 mag
$E(B-V)_{\rm tot}$	0.398 ± 0.002 mag
Peak magnitude ($V_{\rm max}$)	-17.26 ± 0.09 mag
Time of $V_{\rm max}$	MJD 59980.52 ± 0.34
Nickel mass	$0.058 \pm 0.017\ M_{\odot}$
s_{50}	0.37 ± 0.01 mag/50 days
Rise time (V)	8.9 days
$t_{\rm PT}$	101.2 ± 0.3 days

Note.
[a] From shock-cooling fit.

The paper is organized as follows: In Section 2, we present the observations and data reduction process, along with the general properties of the SN. In Section 3, we present our extinction calculations and the analysis we performed on the photometric data to calculate the nickel mass. We also compare our observed light curve with an updated shock-cooling model. Then, we present the spectroscopic analysis showing the presence of a ledge feature and absorption lines on the blue side of Hα and Hβ. We discuss and provide implications of our results and present conclusions in Section 4.

2. Observations and Data Reduction

2.1. Host Galaxy

The host galaxy of SN 2023axu is NGC 2283 at a heliocentric redshift of $z = 0.002805 \pm 0.000005$ (Koribalski et al. 2004). We assume the distance to the host galaxy to be 13.68 ± 2.05 Mpc and a distance modulus of 30.68 mag from the PHANGS survey (Anand et al. 2021). For this distance calculation, Anand et al. (2021) implement the numerical action methods (NAM) model described in Shaya et al. (2017) and Kourkchi et al. (2020). The field of SN 2023axu was observed by ATLAS starting ∼5 yr pre-explosion. We stacked the single-epoch flux measurements in 10-day bins following Young (2022) to reach a deeper limit. There are no precursor outbursts observed with detection limits in o and c down to $\gtrsim -10.5$ mag. Most of the limits for SN 2023axu are fainter than the precursor of SN 2020tlf ($\gtrsim -11.5$ mag) (Jacobson-Galán et al. 2022).

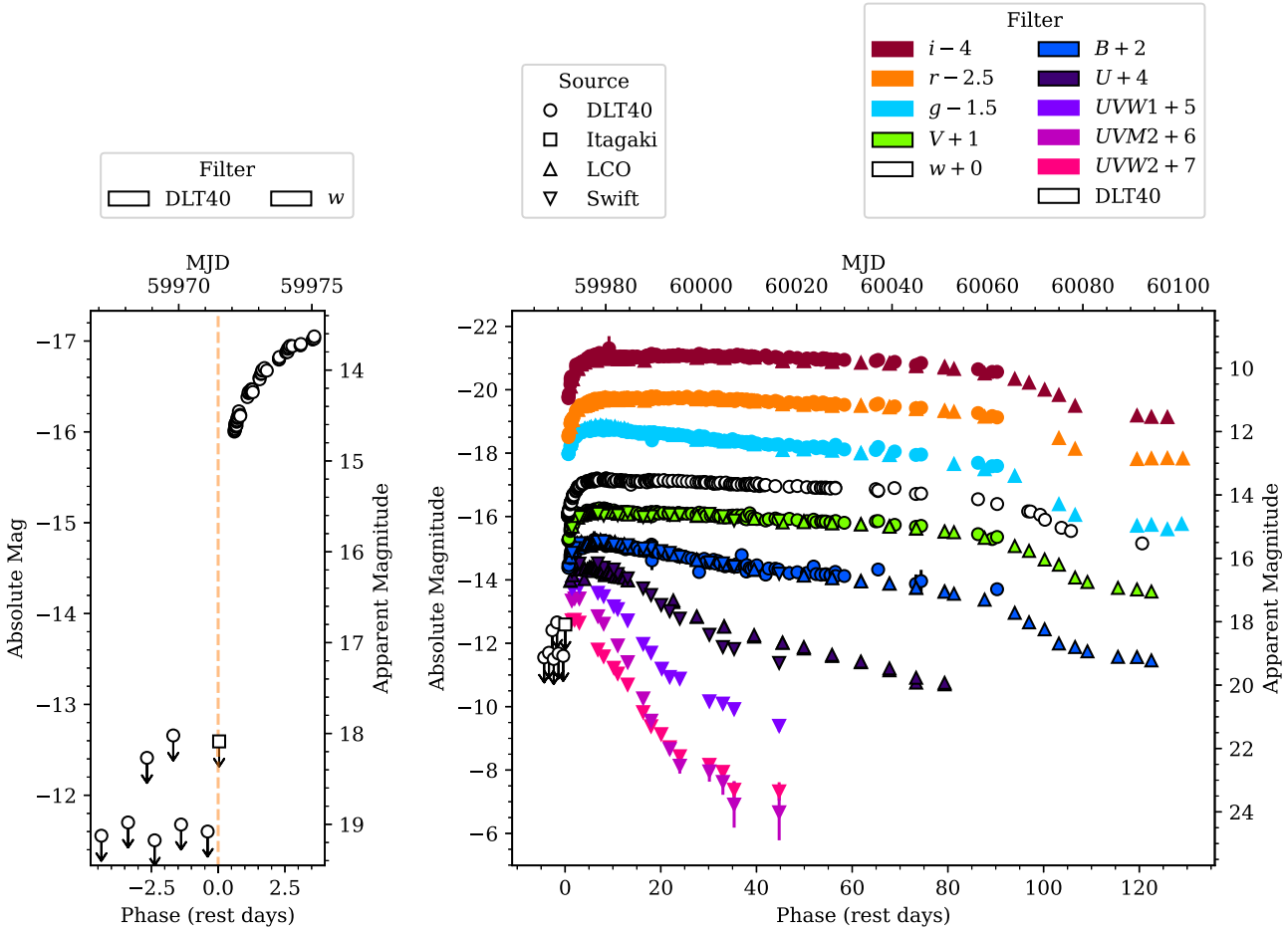

Figure 2. Left: DLT40 clear filter zoom-in of the light curve for the first 10 days after the explosion. Right: multiwavelength photometry in absolute and extinction-corrected ($E(B-V) = 0.398 \pm 0.002$) apparent magnitudes of SN 2023axu spanning the UV to the optical observed using Swift, LCO, and DLT40. The light curve is well sampled throughout the first 150 days, including the rise, plateau, and fall from plateau and nickel tail.

(The data used to create this figure are available.)

2.2. Photometric Follow-up

After discovery, we continued imaging observations of SN 2023axu using DLT40 and the Las Cumbres Observatory network of 1 m telescopes (Brown et al. 2013) via the Global Supernova Project (GSP) with high-cadence photometric observations. In addition, we also triggered the Ultraviolet/Optical Telescope on the Neil Gehrels Swift Observatory (Gehrels et al. 2004) and started observations on MJD 59972.5 a day after the discovery.

Multiband (*BVgri*) and open filter data were taken utilizing SkyNet's network of 0.4 m PROMPT telescopes (Reichart et al. 2005) via the DLT40 project. The *BVgri* filter data were preprocessed using a Python-based pipeline, and aperture photometry was performed. These data are calibrated using the APASS catalog. Open filter data were template subtracted using HOTPANTS (Becker 2015), and magnitudes were calibrated to *r* band. The data from Las Cumbres Observatory were reduced using LCOGTSNPIPE (Valenti et al. 2016), a photometric reduction pipeline based on PyRAF. The APASS catalog was used to calibrate the *BVgri* filters, and the Landolt catalog was used for *U* calibration. Finally, the Swift UVOT data were reduced following the prescription in Brown et al. (2009), and the updated zero-points from Breeveld et al. (2011) were used for the calibration. The light curve from all the instruments is presented in Figure 2.

2.3. Spectroscopic Follow-up

We observed SN 2023axu spectroscopically using various facilities: FLOYDS on Faulkes Telescope North (FTN; Brown et al. 2013) as a part of the GSP; Binospec (Fabricant et al. 2019) on the MMT on Mount Hopkins, Arizona; the Boller and Chivens Spectrograph (B&C) on the Bok 2.3 m telescope located at Kitt Peak National Observatory; the Robert Stobie Spectrograph (RSS) on the Southern African Large Telescope (SALT; Smith et al. 2006); and the Goodman High-Throughput Spectrograph (GHTS; Clemens et al. 2004) on the Southern Astrophysical Research Telescope (SOAR; 4.1 m telescope at Cerro Pachon, Chile). We used our newly developed PyMMT wrapper (described in the Appendix) to trigger rapid spectroscopy with MMT Binospec, obtaining our first spectrum +1.1 days after explosion and the same day as the discovery. A log of spectroscopic observations is presented in Table 2, and the spectral evolution is presented in Figure 3.

The FLOYDS data were reduced using a purpose-built pipeline in IRAF (Valenti et al. 2014). For the Binospec data, the initial data processing of flat-fielding, sky subtraction, and wavelength and flux calibration was done using the Binospec

Table 2
Log of Spectroscopic Observations

Date (UTC)	MJD	Telescope	Instrument	Range (Å)	Exp (s)	Slit (arcsec)
2023-01-28	59972.171	MMT	Binospec	3900–9240	3600	1
2023-01-28	59972.525	FTS	FLOYDS	3500–10000	1800	2
2023-01-30	59974.085	SALT	RSS	3495–9390	1893	1.5
2023-01-31	59975.085	SOAR	GHTS RED	3350–7000	285	1
2023-02-01	59976.466	FTS	FLOYDS	3500–10000	1800	2
2023-02-04	59979.431	FTS	FLOYDS	3500–10000	1799	2
2023-02-05	59980.539	FTS	FLOYDS	3500–10000	1800	2
2023-02-06	59981.489	FTS	FLOYDS	3500–10000	1200	2
2023-02-06	59981.534	FTS	FLOYDS	3500–10000	1200	2
2023-02-09	59984.603	FTS	FLOYDS	3500–10000	1200	2
2023-02-16	59991.538	FTS	FLOYDS	3500–10000	1200	2
2023-02-24	59999.488	FTS	FLOYDS	3500–10000	900	2
2023-03-06	60009.445	FTS	FLOYDS	3500–10000	900	2
2023-03-10	60013.445	MMT	Binospec	5255–7753	1800	1
2023-03-17	60020.410	FTS	FLOYDS	3500–10000	900	2
2023-03-25	60028.249	Bok	B&C	4100–8000	900	1.5
2023-03-26	60029.249	Bok	B&C	4100–8000	900	1.5
2023-03-27	60030.249	FTS	FLOYDS	3500–10000	900	2
2023-04-10	60044.430	FTS	FLOYDS	3500–10000	1500	2
2023-04-21	60055.390	FTS	FLOYDS	3500–10000	1500	2
2023-05-06	60070.353	FTS	FLOYDS	3500–10000	1500	2
2023-05-19	60083.356	FTS	FLOYDS	3500–10000	1800	2

IDL pipeline (Kansky et al. 2019).[20] We then extracted the 1D spectrum using IRAF (Tody 1986, 1993). The B&C spectra were reduced using standard IRAF reduction techniques. The RSS spectra from SALT were reduced using a custom long-slit pipeline based on the PySALT package (Crawford et al. 2010). Finally, Goodman spectra were reduced using a custom Python package developed by SOAR Observatory.[21]

3. Analysis

3.1. Extinction

The equivalent width of the Na ID absorption line is known to correlate with the interstellar dust extinction (Richmond et al. 1994; Munari & Zwitter 1997; Poznanski et al. 2012). We used an MMT Binospec spectrum with a resolving power of 1340 ($\lambda/\delta\lambda$) to fit the equivalent width to the Na I D1 and Na I D2 absorption features, which are clearly separated. We simultaneously fit a Gaussian function to the absorption of both the Milky Way and the host galaxy along with the continuum using the astropy modeling package (Astropy Collaboration et al. 2013; Price-Whelan et al. 2018; Astropy Collaboration et al. 2022). The best-fit equivalent width was used in Equation (9) from Poznanski et al. (2012), and a renormalization factor of 0.86 from Schlafly & Finkbeiner (2011) was applied. This gives $E(B-V) = 0.383 \pm 0.015$ mag for the Milky Way extinction (note: this value of extinction is on the upper end of the Poznanski et al. 2012 sample distribution). This value is in agreement with the Milky Way extinction of $E(B-V) = 0.3319 \pm 0.0107$ from Schlafly & Finkbeiner (2011) from the IPAC Dust Service[22] (IRSA 2022) at the SN 2023axu coordinates. We find a low level of extinction for the host galaxy with $E(B-V) = 0.015 \pm 0.001$ mag. In this paper, we use the Milky Way extinction value calculated using the Na ID absorption line; thus, the total color excess is $E(B-V) = 0.398 \pm 0.015$ mag.

3.2. Photometry

The multiwavelength light curve of SN 2023axu is presented in Figure 2. The light curve evolves as a normal SN II, which can be seen in Figure 4. We perform analysis on SN 2023axu photometric data as done in Valenti et al. (2016) for a sample of SNe II to characterize the light curve. The peak brightness is reached between MJD 59979.59 (+8.2 days) and MJD 59980.92 (+9.5 days), depending on the filter. It has a normal rise time of 8.9 days in the V band for the peak magnitude of −17.26 for an SN II as seen in Valenti et al. (2016; Figure 16, top panel).

The V-band decline rate in the 50 days after the light curve reaches the plateau is denoted by s_{50} and calculated following the prescription of Valenti et al. (2016). For SN 2023axu we find $s_{50} = 0.37 \pm 0.01$ mag/50 days. In Figure 5, we plot the peak in V-band absolute magnitude against s_{50} for SNe II, including SN 2023axu, which falls in the normal range for other SNe of the same class. As expected for normal SNe II, the rise is followed by a plateau phase (t_{PT}, described in Valenti et al. 2016), which lasts for 101.2 ± 0.3 days for SN 2023axu. This value is also in the normal range for an SN II of similar magnitude. In the next section, we use data after the fall from the plateau to calculate the nickel mass.

3.3. Nickel Mass

Toward the end of the data set presented in this paper, SN 2023axu falls from the plateau, as shown in Figure 2, and settles on the radioactive-decay tail. This phase of the SN II is driven by the radioactive decay of nickel to iron ($^{56}\mathrm{Ni} \rightarrow {}^{56}\mathrm{Co} \rightarrow {}^{56}\mathrm{Fe}$). To calculate the nickel mass for SN 2023axu, we use data in B, V, g, r, and i filters. We calculate pseudobolometric luminosity following Valenti et al. (2008). We then compare this pseudobolometric luminosity with the

[20] https://bitbucket.org/chil_sai/binospec/wiki/Home
[21] https://soardocs.readthedocs.io/projects/goodman-pipeline/en/latest/
[22] https://irsa.ipac.caltech.edu/applications/DUST/

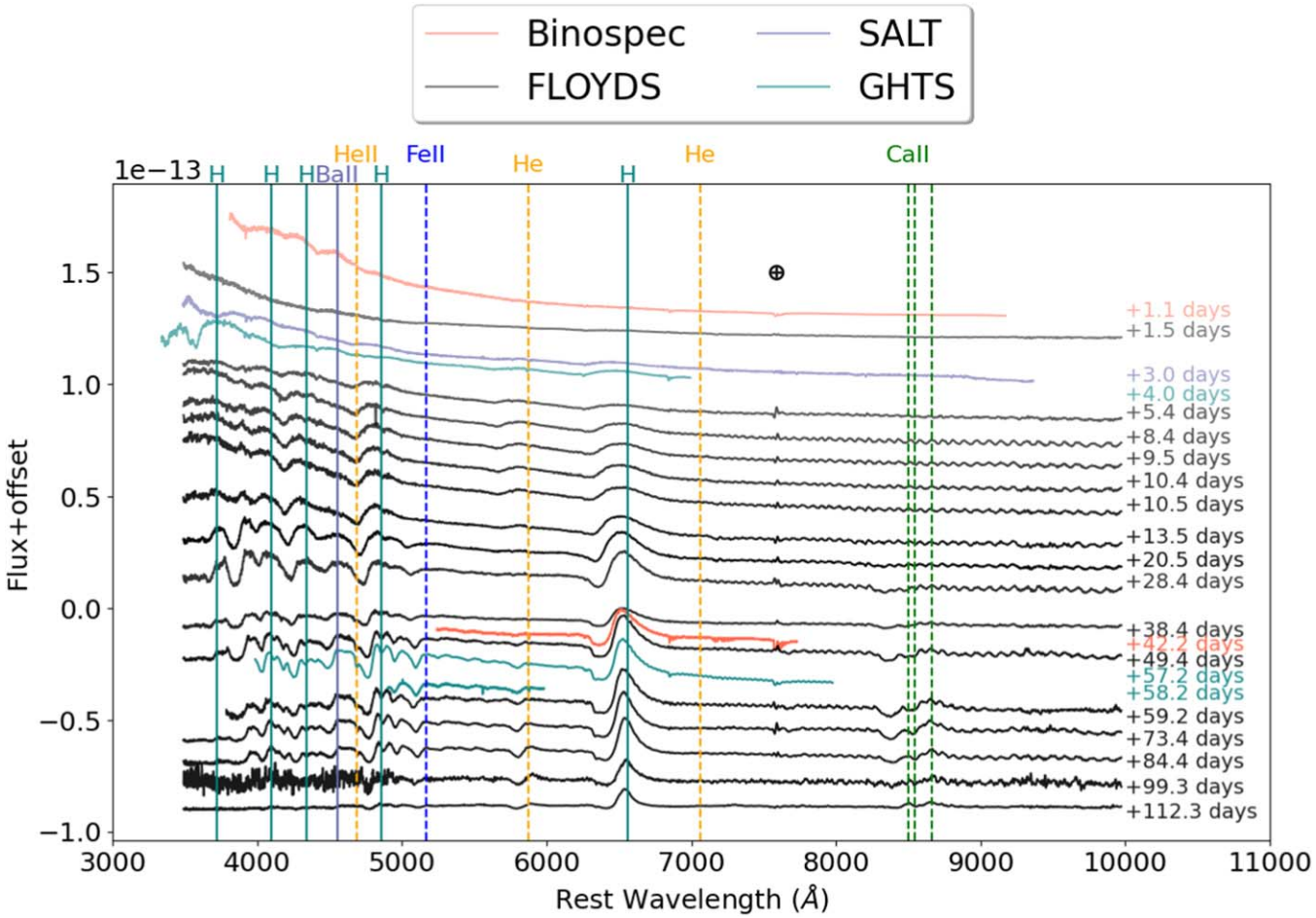

Figure 3. Optical spectral evolution of SN 2023axu starting at +1.1 days after the explosion and ending at +112.3 days. All the spectra are extinction corrected. All spectra will be made available on WISeRep (https://www.wiserep.org).

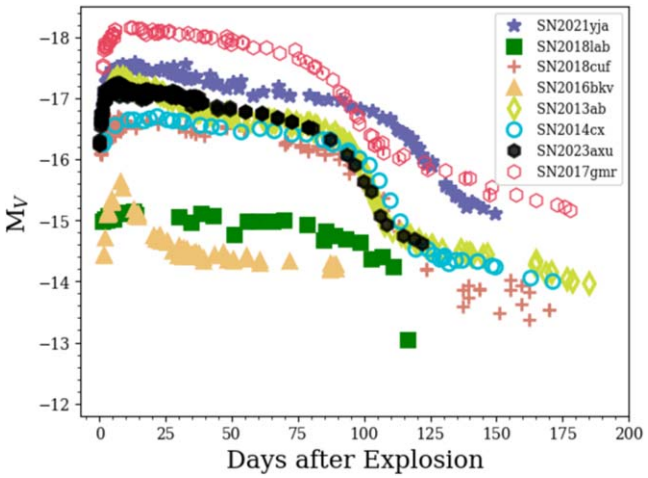

Figure 4. Absolute *V*-band magnitude of SN 2023axu (black) compared to other SNe II: SN 2021yja (Hosseinzadeh et al. 2022), SN 2018lab (Pearson et al. 2023), SN 2018cuf (Dong et al. 2021), SN 2013ab (Bose et al. 2015), SN 2014cx (Huang et al. 2016), and SN 2017gmr (Andrews et al. 2019). The peak *V*-band magnitude of SN 2023axu is −16.53 mag, which is closest to SN 2018cuf and SN 2014cx.

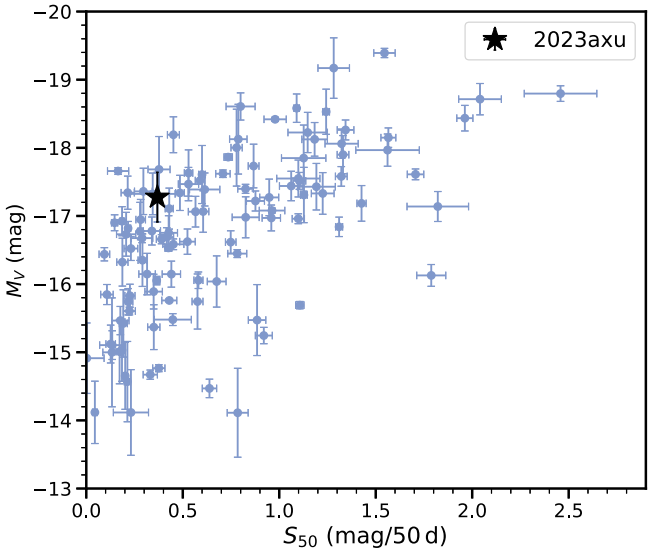

Figure 5. Comparison of *V*-band peak absolute magnitude with respect to slope (mag/(50 days)) with other SNe II from Valenti et al. (2016). The value of SN 2023axu falls in the normal part of the trend seen by Valenti et al. (2016).

pseudobolometric light curve of SN 1987A (*B*, *V*, *g*, *r*, *i*) (we note that for *g*, *r*, *i* Sloan filters, we perform synthetic photometry on SN 1987A spectra) following the method by Spiro et al. (2014); $M_{\rm Ni} = 0.075 M_{\odot} \times \frac{L_{23\rm axu}}{L_{87A}}$, where $L_{23\rm axu}$ and L_{87A} are the pseudobolometric luminosities of SN 2023axu and SN 1987A, respectively. For this calculation to be valid, we assume that the ejecta completely traps the γ-rays produced by the radioactive decay. The pseudobolometric curve for this period declines

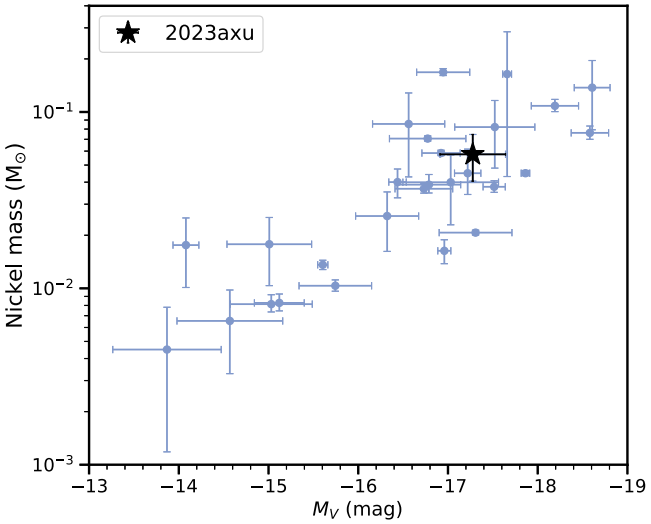

Figure 6. Nickel mass with respect to *V*-band absolute magnitude at 50 days for SN 2023axu (star), along with other SNe II from Valenti et al. (2016). The value of the SN follows the expected trend.

similarly to that of fully trapped ^{56}Co decay of 0.98 mag 100 day^{-1}. To calculate L_{23axu} and L_{87A}, we make use of data from 105 to 125 days after the explosion epoch. Finally, we substitute the calculated L_{23axu} and L_{87A} in $M_{Ni} = 0.075 M_\odot \times \frac{L_{23axu}}{L_{87A}}$ and find an average $M_{Ni} = 0.058^{+0.017}_{-0.017} M_\odot$ for the time period of 105–125 days. A relation between nickel mass and absolute magnitude in the *V*-band SNe II has been found in the literature (e.g., Hamuy 2003; Anderson et al. 2014; Spiro et al. 2014; Valenti et al. 2016). We overplot the value of SN 2023axu in the sample by Valenti et al. (2016) and find it to follow the trend as shown in Figure 6.

3.4. Shock-cooling Model

The early photometric evolution of SNe II is thought to be driven by emission from shock cooling of the stellar envelope, at least in the absence of significant CSM. This form of emission carries the signatures of the progenitors. Hence, modeling this emission using analytic recipes can play an important role in constraining the properties of progenitor stars. With this in mind, we utilized the shock-cooling model of Morag et al. (2023, hereafter MSW23) to model the early light curve of SN 2023axu. We fit this model using the Light Curve Fitting package (Hosseinzadeh et al. 2023). Recently, this model has been successfully implemented for the case of SN 2023ixf (Hosseinzadeh et al. 2023), where a good match to the early light curve was found. In this paradigm, the star is assumed to be a polytrope with a density profile $\rho_0 = \frac{3 f_\rho M}{4\pi R^2} \delta^n$, where f_ρ is a numerical factor of order unity, M is the ejecta mass (with the remaining remnant neglected), R is the stellar radius, $\delta \equiv \frac{R-r}{R}$ is the fractional depth from the stellar surface, and $n = \frac{3}{2}$ is the polytropic index for convective envelopes. The shock velocity profile is described by $v_{sh} = v_{s*} \delta^{-\beta n}$, where v_{s*} is a free parameter and $\beta = 0.191$ is a constant. In the shock-cooling model, we treat $f_\rho M$ as a single parameter because they always appear together and are highly degenerate. The unknown core-collapse explosion time is parameterized by t_0. M_{env} is the mass in the stellar envelope, defined as the region where $\delta \ll 1$. Finally, we also include an intrinsic scatter term σ, which accounts for the scatter around the model, as well as probable underestimates of photometric uncertainties. We multiply the observed error bars by a factor of $\sqrt{1+\sigma^2}$. The Morag et al. (2023) model is built on previous shock-cooling models (Rabinak & Waxman 2011; Sapir et al. 2011; Katz et al. 2012; Sapir et al. 2013; Sapir & Waxman 2017). The model by Sapir & Waxman (2017, hereafter SW17) has identical fit parameters to Morag et al. (2023), with a few key differences. First, they do not account for the very early phase where the thickness of the emitting shell is smaller than the stellar radius. Second, they assume a blackbody spectral energy distribution (SED) at all times, whereas Morag et al. (2023) account for some line blanketing in UV. We fit our observed light-curve data with both SW17 and MSW23 models and compare the results for completeness.

The results of the MSW23 and SW17 shock-cooling models for the early light curve of SN 2023axu and a comparison between the two models are presented in Figure 7, and the best-fit parameters are presented in Table 3. We find that both models converge and give an overall good fit with some significant discrepancies for the observed data in UV filters. We find that the best-fit parameters are reasonably comparable between the two prescriptions. However, the progenitor radius of $417 \pm 28\ R_\odot$ from MSW23 is smaller than $560 \pm 43\ R_\odot$ from SW17; a similar difference has been seen previously by Hosseinzadeh et al. (2023) for SN 2023ixf. We find the error in radius estimate to be lower for MSW23 compared to SW17.

The best-fit model for MSW23 constrains the radius of the progenitor to be $R = 417 \pm 28\ R_\odot$, which falls in a reasonable range for RSGs (100–1500 $R_\odot$; Levesque 2017). We also constrain the explosion time to be $t_0 = 59971.48 \pm 0.03$ (MJD), which is ∼0.7 days before the discovery detection by DLT40 and after the last DLT40 nondetection on MJD 59971.084. We note that the last nondetection from Itagaki is inconsistent with the explosion time from the shock-cooling model and that they would have made a detection at MJD 59971.48 ± 0.03. All the best parameters using Morag et al. (2023), along with comparisons to the Sapir & Waxman (2017) model, are presented in Table 3.

We find minor deviation in *i*, *r* and significant discrepancies in different UV filters. To our knowledge, this is the first time the shock-cooling model of Morag et al. (2023) has been used for a full set of data including UV filters. For SN 2023axu, the *i*, *r* best fit does not rise as quickly as the data. Morozova et al. (2017, 2018) have shown that models without CSM cannot predict this rise well; we note that in their model all the filters require CSM for the steep rise observed. In their model, the presence of dense CSM provides a better fit to the first ∼20 days of the SN II light curves. Thus, the slight excess in the *i*, *r* bands compared to the shock-cooling model could be explained by the presence of CSM. We find that the best fit also underpredicts our observed data for *U*, *UVM*2, and *UVW*2 filters for all epochs. For *UVW*1, the model also underpredicts our observations for later epochs, the phases for which MSW23 modify the SED to account for UV line blanketing. Therefore, this discrepancy in the UV filters for SN 2023axu could be due to Morag et al. (2023) overcorrecting for the line blanketing in the UV.

So far, we do not have any cases where the UV data fit the predictions from the shock-cooling models—recent studies include SN 2018cuf (Dong et al. 2021), SN 2017gmr (Andrews et al. 2019), and SN 2016bkv (Hosseinzadeh et al. 2018),

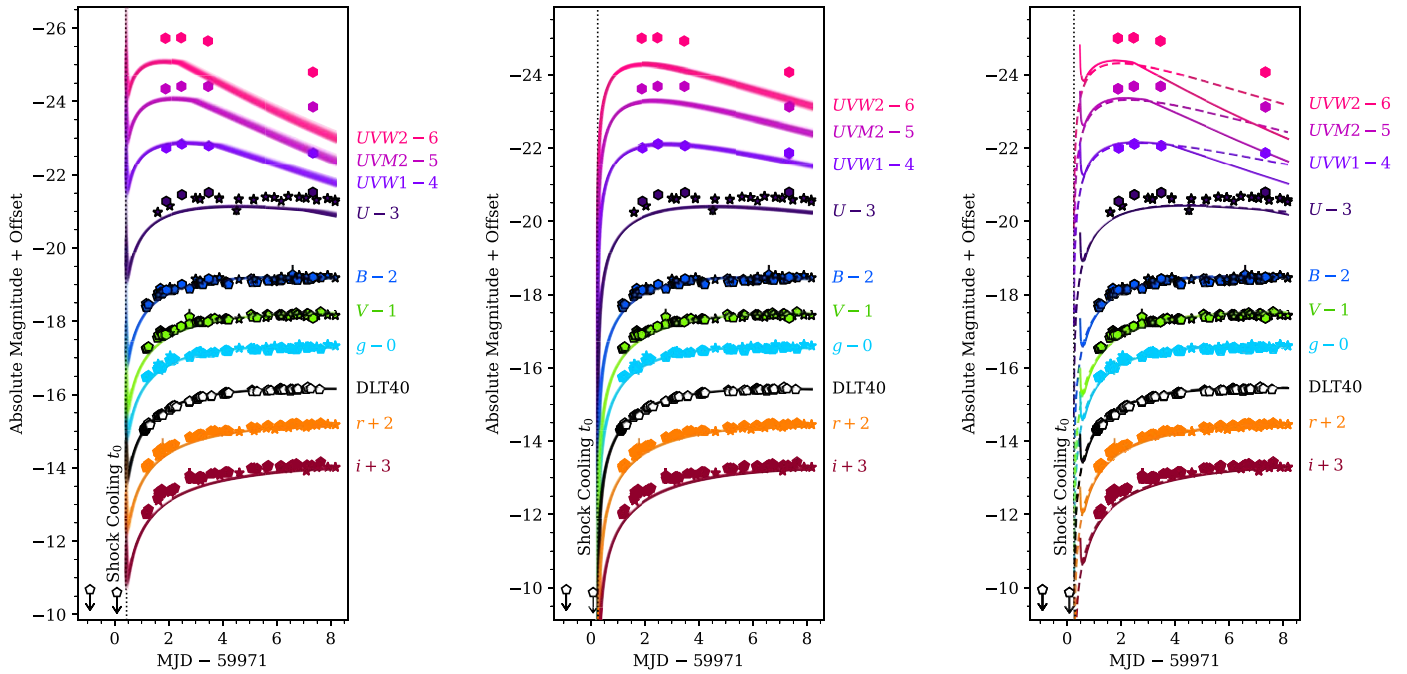

Figure 7. Shock-cooling modeling of SN 2023axu using the prescription of Morag et al. (2023; left) and Sapir & Waxman (2017; middle). The best-fit explosion epoch for each model is shown by a dotted line. The right panel shows the comparison of the models with respect to the observational data. The solid lines are for MSW23 models, and the dashed lines are for SW17 models.

Table 3
Shock-cooling Parameters

Parameter	Variable	Prior			Best-fit Values[a]		Units
		Shape	Min.	Max.	MSW23	SW17	
Shock velocity	v_{s*}	Uniform	0.2	1.5	$1.14^{+0.07}_{-0.06}$	$0.87^{+0.04}_{-0.03}$	$10^{8.5}$ cm s^{-1}
Envelope mass[b]	M_{env}	Uniform	1	3	$1.2^{+0.2}_{-0.1}$	1.2 ± 0.1	$M_\odot$
Ejecta mass × numerical factor	f_ρ M	Uniform	0	1.2	$0.6^{+0.2}_{-0.1}$	0.7 ± 0.2	$M_\odot$
Progenitor radius	R	Uniform	0	1438	417 ± 28	$560 \pm +43$	$R_\odot$
Explosion time	t_0	Uniform	59970	59972.7	59971.48 ± 0.03	$59971.26^{+0.01}_{-0.02}$	MJD
Intrinsic scatter	σ	Log-uniform	0	10^2	5.8 ± 0.2	5.7 ± 0.2	···

Notes.
[a] The "Best-fit Values" columns are determined from the 16th, 50th, and 84th percentiles of the posterior distribution, i.e., median $\pm 1\sigma$. MSW23 and SW17 stand for the two models from Morag et al. (2023) and Sapir & Waxman (2017), respectively. The former is preferred.
[b] See Section 3.4 for the definition of "envelope" in the shock-cooling paradigm.

although these efforts have used the previous version of the shock-cooling prescription (Sapir & Waxman 2017). A systematic effort to model early SN II light curves with the latest shock-cooling models is warranted.

3.5. Spectral Evolution

We present the optical spectral evolution of SN 2023axu in Figure 3 spanning from 1.1 to 112.3 days after the explosion (using the estimated explosion epoch derived from light-curve fitting in Section 3.4). The spectral evolution of SN 2023axu is largely typical for an SN II with P Cygni lines of hydrogen and helium that develop ∼10 days after explosion. We can see the formation of Ba II, Fe II, and Ca II lines at later stages. However, we see two interesting features in our spectra: (1) at early times, before ∼3 days with respect to explosion, we see a "ledge-shaped" feature around 4500–4800 Å; and (2) there is a flat absorption component in the Hα P Cygni profile, along with an additional shallow absorption feature. We discuss these aspects of the spectral evolution in detail below.

3.5.1. Ledge Feature

The "ledge" feature seen around 4600 Å and spanning roughly from 4400 to 4800 Å (Figure 8) is present in the first two epochs of our spectroscopic observations. There is no clear signature of this feature starting +3 days after explosion. This ledge feature has been observed in a few other SNe, for example, SN 2017gmr (Andrews et al. 2019), SN 2018fif (Soumagnac et al. 2020), SN 2018lab (Pearson et al. 2023), SN 2021yja (Hosseinzadeh et al. 2022), and SN 2022acko (Bostroem et al. 2023b). In the literature, this feature has been attributed to circumstellar interactions; however, the interpretation of this interaction is explained in two different ways:

1. Bullivant et al. (2018) and Andrews et al. (2019) explained it as a broad, blueshifted He II λ4686 line

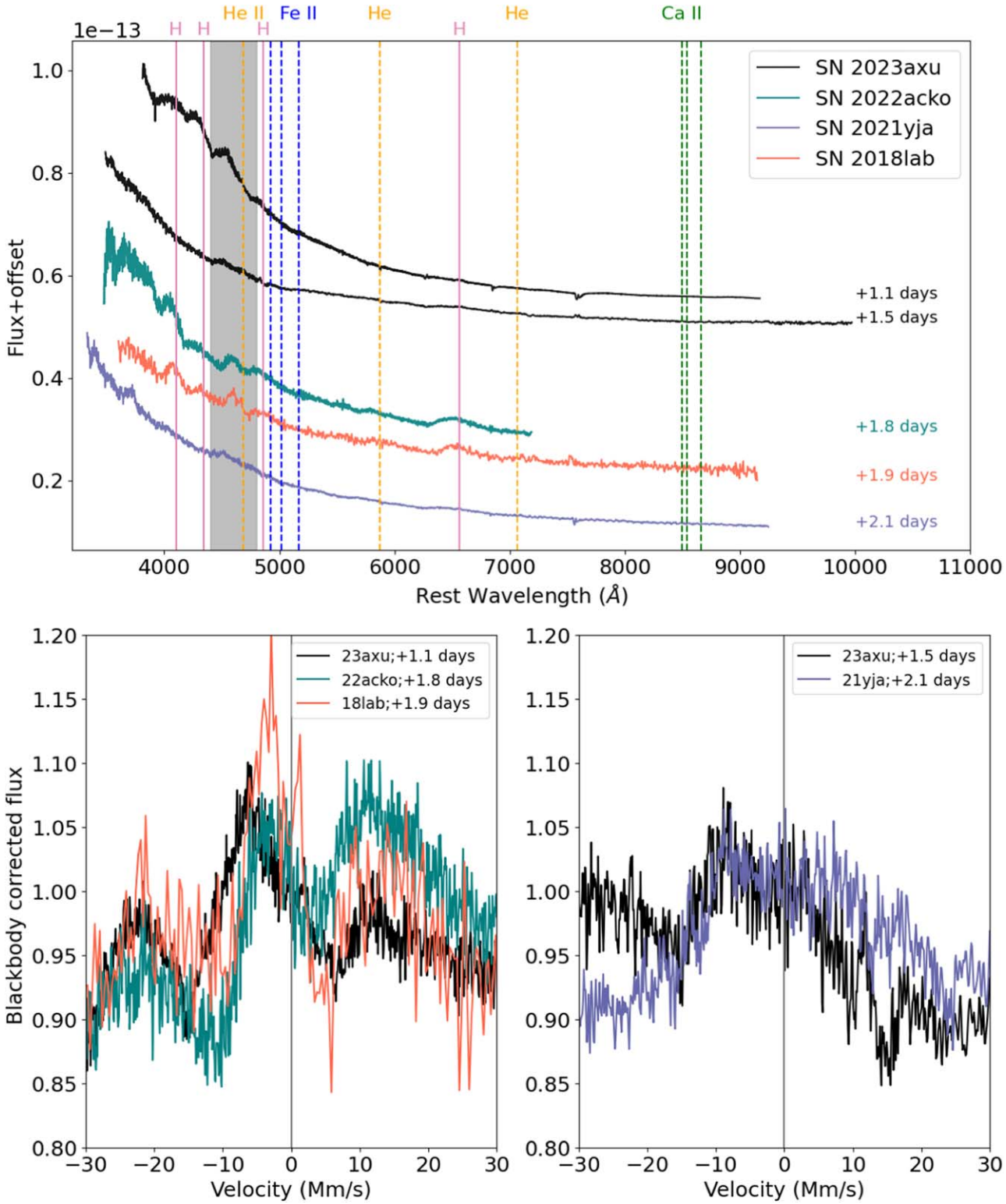

Figure 8. Top: first two epochs of SN 2023axu compared to several other SNe II with observations of "ledge" features, highlighted by the gray shaded region. Bottom: ledge feature present around 4600 Å for SN 2023axu compared to SN 2022acko and SN 2018lab at +1.1 days (left) and SN 2021yja at +1.5 days (right).

that is produced in the outermost layer of SN ejecta beneath a CSM shell.

2. Other papers have attributed this feature to bulk motion creating broad lines and blending of several ionized features from the CSM (Soumagnac et al. 2020; Bruch et al. 2021).

The observation of the ledge feature and lack of prominent emission-line flash features in SN 2023axu add to the spectral diversity of SNe II, although we note the possibility of the presence of flash features in the spectra before our first epoch of observation. In the top panel of Figure 8, we plot the first two epochs of SN 2023axu along with three other SNe II showing

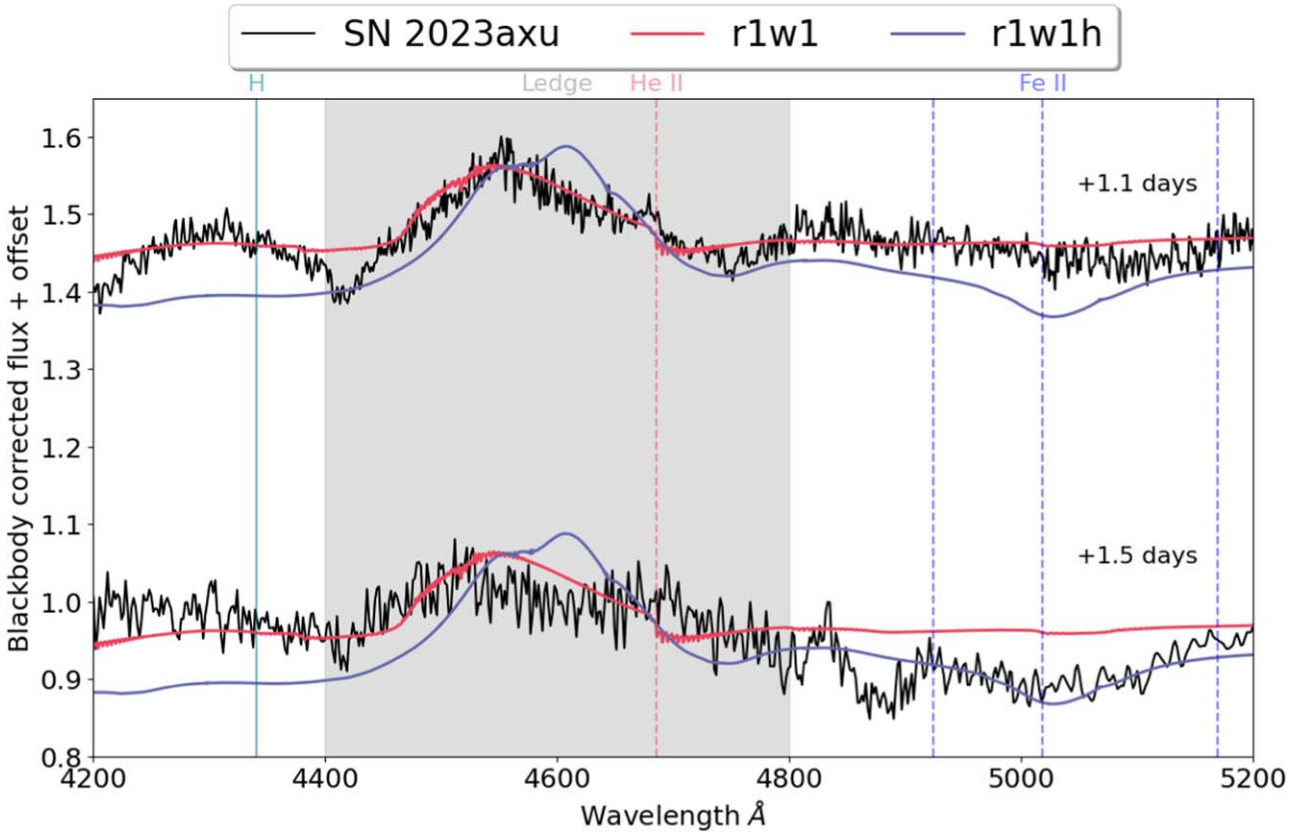

Figure 9. Comparison of the ledge feature of SN 2023axu at +1.1 and +1.5 days with models at +1.0 days for `r1w1` and at +1.6 days for `r1w1h` by Dessart et al. (2017). Both models are for RSGs with CSM, and model `r1w1h` is with extended atmospheres. The gray shaded region indicates the approximate wavelength range for the ledge feature.

the ledge feature. We zoom in on the ledge feature in the bottom panel, where we have plotted a continuum-normalized flux for this feature in comparison to a few other SNe for the first and second epochs of spectroscopic observations (+1.1 and +1.5 days, respectively). We find that for the first epoch the ledge feature of SN 2023axu behaves similarly to that seen in SN 2018lab and SN 2022acko (Figure 8, left), both of which are low-luminosity SNe II. For the second epoch, the shape of the feature is very similar to that seen for SN 2021yja, a UV-bright SN II (Figure 8, right). This implies that the diversity of this feature may be due to the rapid temporal evolution of which we only have sparse sampling rather than the intrinsic properties of the SN itself.

We also compared this feature with radiation transfer simulations by Dessart et al. (2017), where they model spectra and light curves for an RSG with a radius of $R_\star = 501\ R_\odot$ that explodes in a low-density CSM of $\dot{M} = 10^{-6}\ M_\odot\ \mathrm{yr}^{-1}$ (the `r1w1` model). The same model as `r1w1` but with the addition of an extended atmosphere with a scale height of $H\rho = 0.3R_\star$ is called `r1w1h`. The comparison of the first two epochs of spectra showing the ledge feature to the `r1w1` and `r1w1h` models is shown in Figure 9. There is no model that fits both of the epochs well. The peak of the `r1w1h` model is distinct from any feature seen in SN 2023axu; however, the model `r1w1` seems to be qualitatively better matched to the morphology of the SN 2023axu ledge feature seen at +1.1 days. This preference suggests that the CSM around SN 2023axu is of low density, which may be the reason why we do not see narrow emission line flash features.

3.5.2. Hα and Cachito Feature

The P Cygni Hα feature develops ∼10 days after explosion as seen in Figure 3. The Hα absorption feature broadens and develops into a square trough after ∼28 days. The ratio of the equivalent width of the absorption to emission (a/e) components at +28.4 days is 0.19. We also calculate the Hα velocity (full-width half maximum of the emission) at the same epoch and found it to be 8770 km s^{-1}. The relation between a/e with respect to Hα velocity has been explored in Gutiérrez et al. (2014), who found the cases with smaller a/e to have higher velocities. We compared the value from SN 2023axu with their sample and found it to fall in the normal range.

There is an additional shallow absorption line of unclear origin within this broad feature at ∼10,000 km s^{-1}, starting at +49 days. Similar absorption components have been seen in other SNe, such as SN 2007X, SN 2004fc, SN 20023hl, SN 1992b, (Gutiérrez et al. 2017), and SN 2020jfo (Teja et al. 2022); this is often dubbed the "Cachito" feature (Gutiérrez et al. 2017).

From a large sample study, Gutiérrez et al. (2017) found that SNe with a Cachito line can be divided into two groups, depending on when the feature is present. In the first group, it is seen around 5–7 days between 6100 and 6300 Å and disappears at ∼35 days. For the second group, the feature appears after 40 days, is closer to Hα (between 6250 and 6450 Å), and can last until ∼120 days. Gutiérrez et al. (2017) found that Cachito features appearing before 40 days after explosion are due to Si II λ6355 for 60% of the cases, and for the rest it is likely due to high-velocity (HV) Hα. For the SNe that have the Cachito

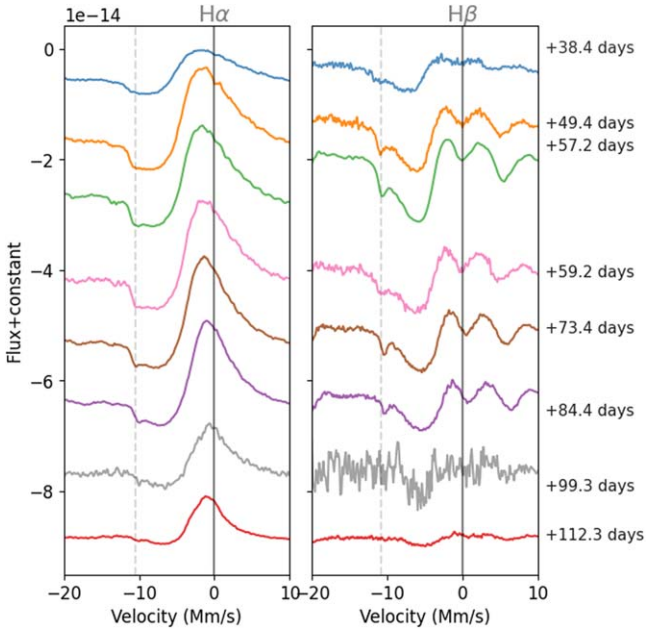

Figure 10. Evolution of the Cachito feature for Hα (left) and Hβ (right) shown by the dashed vertical line. The velocity is calculated with respect to Hα λ6562.8 and Hβ λ4861, shown with gray lines. The shallow absorption feature is seen for both Hα and Hβ at a very similar velocity.

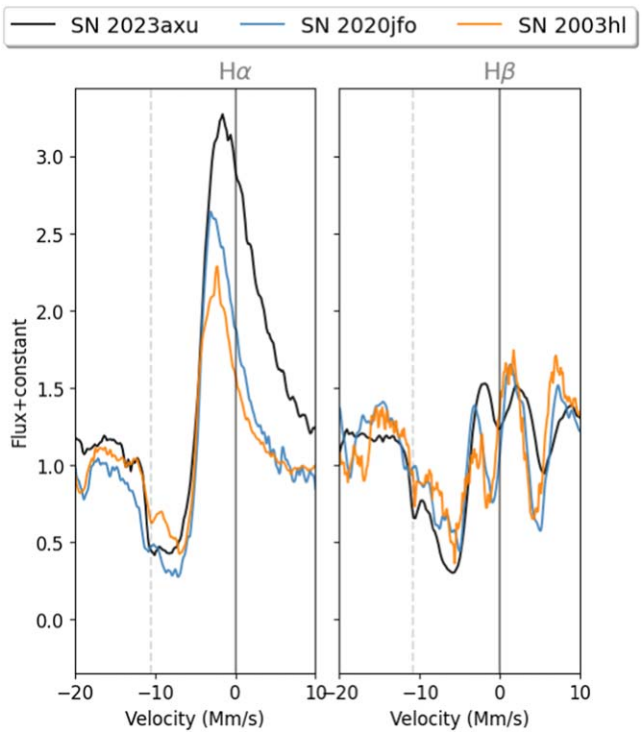

Figure 11. Comparison of the Cachito feature in SN 2023axu for Hα (left) and Hβ (right), shown by the dashed vertical line, with those in SN 2020jfo and SN 2003hl. The epochs of observation are +57.2, +55, and +63 days for SN 2023axu, SN 2020jfo, and SN 2003hl, respectively. The velocity is calculated with respect to Hα λ6562.819 and Hβ λ4861, shown with the gray solid line. The overall feature of SN 2023axu is similar to those of SN 2020jfo and SN 2003hl.

feature 40 days after explosion, Chugai et al. (2007) have shown that the feature is due to HV H absorption. SN 2023axu falls in the latter category, where the feature develops after 40 days as seen in Figure 3. For this category of SNe, Gutiérrez et al. (2017) found that a similar shallow absorption feature is seen on the blue side of Hβ, which we find in our spectrum as well. The time-series evolution of this feature is shown in Figure 10.

Though the SN 2023axu Cachito feature develops after 40 days, and this is usually attributed to an HV H feature, we explored the possibility of a Si II λ6355 (Valenti et al. 2014) or Ba II λ6497 origin. If the feature is arising owing to Si II λ6355, then the line velocity inferred is closer to a few hundred kilometers per second. On the other hand, if we assume that the Ba II λ6497 line is producing the feature, then we infer the velocity to be $\sim$7500 km s^{-1}. Both of these velocities are different from the velocity inferred from the Fe II λ5169 line ($\sim$4000 km s^{-1}). In addition, we also find shallow absorption features on the blue side of Hβ; hence, we disfavor this possibility.

Finally, we checked whether HV H, which originates when X-rays from the SN shock ionize and excite the outer shocked ejecta (Chugai et al. 2007), can explain this feature. We find this feature in SN 2023axu 40 days after explosion, and there is a similar feature on the blue side of Hβ at a similar velocity ($\sim$10,500 km s^{-1}) to the Hα case, i.e., $\sim$10,000 km s^{-1}. This velocity is comparable to the velocity we derived for Hα at +28 days after the explosion. Gutiérrez et al. (2017) found that 43 out of 122 SNe II show the Cachito later than 40 days in their sample, and 63% of them also have a counterpart in Hβ. They find that HV H explains the feature the best. In addition, Kilpatrick et al. (2023) and Teja et al. (2022) found a similar feature for another SN II, SN 2020jfo, and Teja et al. (2022) attributed it to HV H as well. Interestingly, SN 2020jfo also contains a broad ledge feature at the first epoch of observation (+3 days). Teja et al. (2022) attribute this feature to high ionization of the ejecta and the nearby CSM. In Figure 11, we find similarities in the Hα absorption shape of SN 2023axu to those of SN 2020jfo and SN 2003hl (Gutiérrez et al. 2017). While the absorption feature in Hβ is not seen for SN 2020jfo, it is present in the spectra of SN 2003hl and is similar to that seen in SN 2023axu. Hence, we favor the HV H scenario for the Cachito feature seen in SN 2023axu.

4. Discussions and Conclusion

In this paper, we present the photometric and spectroscopic data analysis of SN 2023axu. The SN was discovered by DLT40 within 24 hr of the explosion in NGC 2283 at a distance of 13.68 Mpc, and prompt spectroscopic follow-up using PyMMT and other instruments enabled us to obtain a spectrum at +1.1 days after the explosion. The SN is a typical Type II with an absolute peak V-band magnitude -17.26 and a plateau phase lasting 101 days. Our observations extended into the radioactive tail phase, allowing us to calculate the nickel mass by comparing the pseudobolometric light curve of SN 2023axu with SN 1987A. We found the nickel mass to be $0.058 \pm 0.017\ M_{\odot}$. This value is within a typical range for SNe II of $0.003-0.17\ M_{\odot}$ (Valenti et al. 2016).

We also performed Markov Chain Monte Carlo shock-cooling fitting to the early light curve of SN 2023axu following the prescription by Morag et al. (2023) and implemented by Hosseinzadeh et al. (2023). We find the model to converge; however, the model underpredicts the signal for the UV data and the model slightly underpredicts the steep rise in the r, i filters. The observed excess flux could be attributed to CSM interaction. From our light-curve analysis with shock-cooling

models we find the progenitor radius to be $417 \pm 28\ R_{\odot}$, implying an RSG progenitor (Levesque 2017). RSGs are known for mass loss during their lifetime. There is increasing evidence of the presence of CSM in many SNe II via the presence of a steep rise in their light curves that cannot be explained by shock-cooling models that assume a lack of CSM. Morozova et al. (2017, 2018) found that the presence of dense CSM in their numerical setup can accurately model the observed early steep rise in the light curve.

We also present high-cadence optical spectra starting at +1.1 to +112.3 days after the explosion epoch. In general, the spectral evolution is typical for SNe II with two notable features: (1) The first two epochs of spectra show the ledge feature at 4400–4800 Å. The ledge feature has been seen in other SNe II (e.g., Andrews et al. 2019; Hosseinzadeh et al. 2022; Bostroem et al. 2023b; Pearson et al. 2023) and has been attributed to the presence of CSM (e.g Soumagnac et al. 2020; Bruch et al. 2021). We also compared this behavior to models by Dessart et al. (2017) and found that the `r1w1` model with a low-density CSM and $\dot{M} = 10^{-6}\ M_{\odot}\ \mathrm{yr}^{-1}$ behaves closest to the observed early spectra of SN 2023axu. (2) At epochs >40 days, we see shallow absorption features on the blue side of Hα and Hβ, and we interpret this as HV H. Chugai et al. (2007) proposed this feature to be the result of the interaction between the SN ejecta and the RSG wind, thus implying the presence of CSM interaction for the case of SN 2023axu. Both spectroscopic and photometric features point to the most likely scenario of an explosion of an RSG surrounded by low-density CSM for SN 2023axu. The steep rise in the early light curve and ledge features in early spectra probe the mass loss from RSG in the final phases before the explosion, whereas the Cachito feature probes the CSM produced by RSG mass loss earlier in its evolution. This work adds to the growing evidence of the presence of CSM around the progenitors of SNe II.

The combination of high-cadence multiwavelength photometric and rapid spectroscopic data helped us constrain the properties of SN 2023axu, including the likely presence of CSM. These results show the need for high-cadence photometric observations of SNe II, along with infrastructure for rapid spectroscopic follow-up. Implementing infrastructure like PYMMT is critical to improving our understanding of the final stages of RSG evolution to SN.

Acknowledgments

Time-domain research by the University of Arizona team, M. S., and D.J.S. are supported by NSF grants AST-1821987, 1813466, 1908972, 2108032, and 2308181, and by the Heising-Simons Foundation under grant No. 2020-1864. K.A.B. is supported by an LSSTC Catalyst Fellowship; this publication was thus made possible through the support of grant 62192 from the John Templeton Foundation to LSSTC. The opinions expressed in this publication are those of the authors and do not necessarily reflect the views of LSSTC or the John Templeton Foundation. Research by Y.D., S.V., N.M.R., E.H., and D.M. is supported by NSF grant AST-2008108. This research has made use of the NASA Astrophysics Data System (ADS) Bibliographic Services and the NASA/IPAC Infrared Science Archive (IRSA), which is funded by the National Aeronautics and Space Administration and operated by the California Institute of Technology. This research made use of Photutils, an Astropy package for the detection and photometry of astronomical sources (Bradley et al. 2019). This work made use of data supplied by the UK Swift Science Data Centre at the University of Leicester. Observations reported here were obtained at the MMT Observatory, a joint facility of the University of Arizona and the Smithsonian Institution. Based in part on observations obtained at the Southern Astrophysical Research (SOAR) telescope, which is a joint project of the Ministério da Ciência, Tecnologia e Inovações (MCTI/LNA) do Brasil, the US National Science Foundation's NOIRLab, the University of North Carolina at Chapel Hill (UNC), and Michigan State University (MSU). This research has made use of the CfA Supernova Archive, which is funded in part by the National Science Foundation through grant AST 0907903. This work makes use of data taken with the Las Cumbres Observatory global telescope network. The LCO group is supported by NSF grants 1911225 and 1911151. J.E.A. and C.E.M.V. are supported by the international Gemini Observatory, a program of NSF's NOIRLab, which is managed by the Association of Universities for Research in Astronomy (AURA) under a cooperative agreement with the National Science Foundation, on behalf of the Gemini partnership of Argentina, Brazil, Canada, Chile, the Republic of Korea, and the United States of America. J.A.C-B. acknowledges support from FONDECYT Regular N 1220083. The SALT data presented here were obtained via Rutgers University program 2022-1-MLT-004 (PI: S.W.J.). L.A.K. acknowledges support by NASA FINESST fellowship 80NSSC22K1599.

Facilities: ADS, MMT (Binospec), LCOGT, SOAR (GHTS), SALT (RSS), NED, IRSA.

Software: astropy (Astropy Collaboration et al. 2013; Price-Whelan et al. 2018; Astropy Collaboration et al. 2022), Photutils (Bradley et al. 2019), Binospec IDL (Kansky et al. 2019), Panacea, BANZAI (McCully et al. 2018), Light Curve Fitting (Hosseinzadeh & Gomez 2020), MatPLOTLIB (Hunter 2007), NumPy (Harris et al. 2020), Scipy (Virtanen et al. 2020), IRAF (Tody 1986, 1993), PySALT (Crawford et al. 2010).

Appendix
PyMMT

We are in the era of focused and general-purpose time domain surveys, which have led to an explosion in the number of transients discovered on a nightly basis; however, most of them do not receive any spectroscopic follow-up or classification (see the extensive discussion in Kulkarni 2020). For various science cases such as young SNe, kilonovae candidates, etc., there is an acute need for nearly real-time spectroscopic observations. To decrease the gap between discovery and spectroscopic response, various robotic spectrographs, such as (a) twin robotic FLOYDS spectrographs on the Faulkes Telescope North & South (Brown et al. 2013), (b) the Spectrograph for the Rapid Acquisition of Transients on the Liverpool Telescope (SPRAT; Piascik et al. 2014), and (c) the Spectral Energy Distribution Machine on the Palomar 60 in telescope (SEDM; Blagorodnova et al. 2018), have been deployed on 2 m class telescopes capable of rapid target-of-opportunity (ToO) observations. When the sources are fainter or we need a better signal-to-noise ratio, a larger aperture size is needed. Several large facilities, such as the South African Large Telescope (SALT), Keck Observatory, the two Gemini

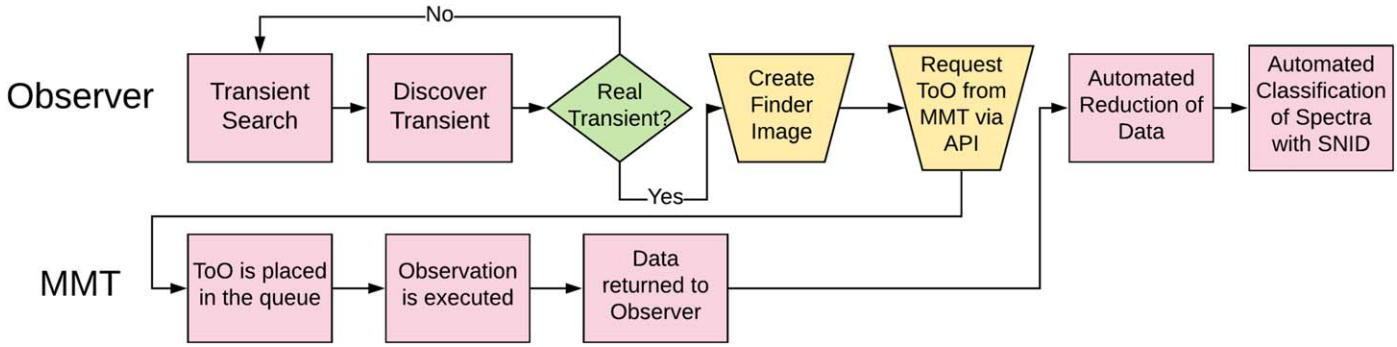

Figure 12. Flowchart for transient identification, MMT+Binospec+MMIRS triggering, and initial analysis for our program.

telescopes (Roth et al. 2009), and SOAR, have rapid ToO programs in place for this purpose.

The 6.5 m MMT[23] can potentially play an important role in the rapid follow-up of transients. The observatory has been mostly operating in a queue mode in observing blocks for the past several years for three spectrographs: Binospec, an optical spectrograph (Fabricant et al. 2019); MMIRS, a near-IR spectrograph (McLeod et al. 2012); and Hectospec, a multi-object optical spectrograph (Fabricant et al. 2005).

Even though the potential for real-time spectroscopic follow-up with MMT is great, the infrastructure is designed for interactive use, and we desire a programmatic interface to upload observations and retrieve data. Currently, in order to request an urgent observation, the observer needs to navigate multiple web pages and optionally submit a finding chart before submitting for the queue. In addition, the observed raw data are not available until the next morning, which can be crucial for certain science cases. All of these extra steps slow down the activation of a ToO request. Hence, we have developed PyMMT (Wyatt et al. 2023), a Python package that communicates with the MMT scheduling software's application programming interface (API; Gibson & Porter 2018), allowing direct, seamless injection of new targets into the observation queue for rapid follow-up. Currently, PyMMT has the capability to trigger Binospec and MMIRS. The workflow of PyMMT is shown in Figure 12.

PyMMT communicates with four endpoints of the MMT API. Each is encapsulated in a Python class. Note that, for all classes (except `Instruments`; Appendix A.2), the user must provide an API token for access control, either by setting the `token` keyword at initialization or by setting the `MMT_API_TOKEN` environment variable. We briefly describe the functionality of each class below. For full documentation, see the `README.md` file in GitHub.[24]

A.1. Requesting Observations

The `Target` class allows the user to submit observation requests to the queue and query their status.[25] It contains validation routines for requested configurations on the two supported instruments, Binospec and MMIRS. To initialize a new `Target` instance, the user first assembles a payload containing the name, coordinates, and brightness of the target, along with instrument-specific configuration parameters. An example MMIRS spectroscopy payload is shown below:

```
payload={
 # target details
 'objectid': 'SN2023axu',
 'ra': '06:45:55.320',
 'dec': '-18:13:53.50',
 'epoch': 'J2000',
 'magnitude': 21.,

 # scheduling details
 'notes': 'Demo observation request.',
 'priority': 3,
 'targetofopportunity': 0,
 'visits': 1,

 # instrument and mode specification
 'instrumentid': 15,
 'observationtype': 'longslit',
 # instrument-specific configuration
 'dithersize': '5',
 'exposuretime': 450.,
 'filter': 'zJ',
 'gain': 'low',
 'grism': 'J',
 'maskid': 111,
 'numberexposures': 3,
 'readtab': 'ramp_4.426',
 'slitwidth': '1pixel',
 'slitwidthproperty': 'long',
}
```

If a target has already been submitted, its details can be retrieved from the MMT API by providing only its ID number, e.g., `payload={'targetid': 14294}`.

The `Target` instance is then initialized with `target=pymmt.Target(payload=payload)`. If a target ID is provided in the payload, details of the already-submitted target will be retrieved from the MMT API immediately on initialization, or they can be retrieved manually with `target.get()`. Validation is also run immediately on initialization, or it can be run manually with `target.validate()`. If any of the provided parameters are invalid, an error message will be printed to the screen. At any point, the parameters can be printed to the screen with `target.dump()`. The target can be submitted to the MMT API with `target.post()`. A finder chart, which is used for MMIRS spectroscopic observations, can be uploaded with, e.g., `target.upload_finder('/path/to/finder.png')`.

[23] http://www.mmto.org

[24] https://github.com/SAGUARO-MMA/PyMMT

[25] In the language of the MMT API, a "target" is not a unique pair of coordinates, but rather a unique request for an observation of a pair of coordinates. One might submit multiple "targets" corresponding to the same SN, for example, to obtain a series of observations at different times or with different configurations, such as different filters or gratings.

Updated target parameters can be sent to the API with, e.g., `target.update(magnitude=22.)`. A target can be deleted (i.e., the observation request can be canceled) with `target.delete()`. Finally, data for a target can be downloaded with `target.download_exposures()` (see also Appendix A.3 below). The data will appear in the `data` subdirectory of the current working directory, e.g., `./data/SN2023axu/D2023.0403/FITS Image/`.

A.2. Viewing the Schedule

The `Instruments` class retrieves and parses the MMT schedule, so users can see which instrument is available on a given night. Because the schedule is public, no API token is required. After initializing an `Instruments` instance with `insts=pymmt.Instruments()`, the schedule can be queried either by instrument or by date. A call to `insts.get_instruments(instrumentid=16)` will return a list of schedule entries indicating when Binospec is on the telescope, as well as print them to the screen. Each entry includes the instrument ID (`'instrumentid'`), program name (`'name'`), and start and end times (`'start'` and `'end'`), given as Python `datetime` instances. A call to `insts.get_instruments(date=datetime(2023, 11, 7))` will return and print the schedule entry for the given date and time. A call to `insts.get_instruments()` with no arguments returns and prints the currently active program.

A.3. Retrieving Data

After observations are obtained, users can view their metadata using the `Datalist` class. After initializing a `Datalist` instance with `datalist=pymmt.Datalist()`, a list of raw data products for a given target can be obtained with, e.g., `datalist.get(targetid=14294)`. Reduced data products can be substituted by giving the keyword argument `data_type='reduced'`. Metadata for these products are stored in the `datalist.data` attribute. When initializing an already-observed `Target`, metadata are automatically stored in the `target.datalist.data` attribute.

Users can download their data using the `Image` class. After initializing an `Image` instance with `im=pymmt.Image()`, a single data product can be downloaded to a local file `'data.fits'` using `im.get(datafileid=fid, filepath='data.fits')`, where `fid` is the ID number of the data product from, e.g., `datalist.data[0]['id']`. We recommend using the higher-level `target.download_exposures()` (Appendix A.1) for downloading raw data of a target in bulk.

ORCID iDs

Manisha Shrestha https://orcid.org/0000-0002-4022-1874
Jeniveve Pearson https://orcid.org/0000-0002-0744-0047
Samuel Wyatt https://orcid.org/0000-0003-2732-4956
David J. Sand https://orcid.org/0000-0003-4102-380X
Griffin Hosseinzadeh https://orcid.org/0000-0002-0832-2974
K. Azalee Bostroem https://orcid.org/0000-0002-4924-444X
Jennifer E. Andrews https://orcid.org/0000-0003-0123-0062
Yize Dong (董一泽) https://orcid.org/0000-0002-7937-6371
Emily Hoang https://orcid.org/0000-0003-2744-4755
Daryl Janzen https://orcid.org/0000-0003-0549-3281
Jacob E. Jencson https://orcid.org/0000-0001-5754-4007
Michael Lundquist https://orcid.org/0000-0001-9589-3793
Nicolás Meza Retamal https://orcid.org/0000-0002-7015-3446
Stefano Valenti https://orcid.org/0000-0001-8818-0795
Jillian C. Rastinejad https://orcid.org/0000-0002-9267-6213
Joannah Hinz https://orcid.org/0000-0003-3339-0546
Benjamin Weiner https://orcid.org/0000-0001-6065-7483
G. Grant Williams https://orcid.org/0000-0002-3452-0560
Daichi Hiramatsu https://orcid.org/0000-0002-1125-9187
D. Andrew Howell https://orcid.org/0000-0003-4253-656X
Curtis McCully https://orcid.org/0000-0001-5807-7893
Estefania Padilla Gonzalez https://orcid.org/0000-0003-0209-9246
Craig Pellegrino https://orcid.org/0000-0002-7472-1279
Giacomo Terreran https://orcid.org/0000-0003-0794-5982
Joseph Farah https://orcid.org/0000-0003-4914-5625
Saurabh W. Jha https://orcid.org/0000-0001-8738-6011
Lindsey Kwok https://orcid.org/0000-0003-3108-1328
Nathan Smith https://orcid.org/0000-0001-5510-2424
Michaela Schwab https://orcid.org/0009-0002-5096-1689
Jeonghee Rho https://orcid.org/0000-0003-3643-839X
Yi Yang https://orcid.org/0000-0002-6535-8500

References

Anand, G. S., Lee, J. C., Van Dyk, S. D., et al. 2021, MNRAS, 501, 3621
Anderson, J. P., González-Gaitán, S., Hamuy, M., et al. 2014, ApJ, 786, 67
Andrews, J. E., Sand, D. J., Valenti, S., et al. 2019, ApJ, 885, 43
Astropy Collaboration, Price-Whelan, A. M., Lim, P. L., et al. 2022, ApJ, 935, 167
Astropy Collaboration, Robitaille, T. P., Tollerud, E. J., et al. 2013, A&A, 558, A33
Beasor, E. R., Davies, B., Smith, N., et al. 2020, MNRAS, 492, 5994
Becker, A., 2015 ASCL, Astrophysics Source Code Library, ascl:1504.004
Blagorodnova, N., Neill, J. D., Walters, R., et al. 2018, PASP, 130, 035003
Bose, S., Valenti, S., Misra, K., et al. 2015, MNRAS, 450, 2373
Bostroem, K. A., Brink, T. G., Filippenko, A. V., et al. 2023a, TNSCR, 2023-230, 1
Bostroem, K. A., Dessart, L., Hillier, D. J., et al. 2023b, ApJL, 953, L18
Bostroem, K. A., Pearson, J., Shrestha, M., et al. 2023c, ApJL, 956, L5
Bradley, L., Sipőcz, B., Robitaille, T., et al. 2019, astropy/photutils: v0.6, Zenodo, doi:10.5281/zenodo.2533376
Breeveld, A. A., Landsman, W., Holland, S. T., et al. 2011, in AIP Conf. Ser. 1358, Gamma Ray Bursts 2010, ed. J. E. McEnery, J. L. Racusin, & N. Gehrels (Melville, NY: AIP), 373
Brown, P. J., Holland, S. T., Immler, S., et al. 2009, AJ, 137, 4517
Brown, T. M., Baliber, N., Bianco, F. B., et al. 2013, PASP, 125, 1031
Bruch, R. J., Gal-Yam, A., Schulze, S., et al. 2021, ApJ, 912, 46
Bruch, R. J., Gal-Yam, A., Yaron, O., et al. 2023, ApJ, 952, 119
Bullivant, C., Smith, N., Williams, G. G., et al. 2018, MNRAS, 476, 1497
Chugai, N. N., Chevalier, R. A., & Utrobin, V. P. 2007, ApJ, 662, 1136
Clemens, J. C., Crain, J. A., & Anderson, R. 2004, Proc. SPIE, 5492, 331
Crawford, S. M., Still, M., Schellart, P., et al. 2010, Proc. SPIE, 7737, 773725
Dessart, L., Hillier, D. J., & Audit, E. 2017, A&A, 605, A83
Dong, Y., Valenti, S., Bostroem, K. A., et al. 2021, ApJ, 906, 56
Ekström, S., Georgy, C., Eggenberger, P., et al. 2012, A&A, 537, A146
Fabricant, D., Fata, R., Epps, H., et al. 2019, PASP, 131, 075004
Fabricant, D., Fata, R., Roll, J., et al. 2005, PASP, 117, 1411
Gal-Yam, A., Arcavi, I., Ofek, E. O., et al. 2014, Natur, 509, 471
Gehrels, N., Chincarini, G., Giommi, P., et al. 2004, ApJ, 611, 1005
Gibson, J. D., & Porter, D. 2018, Proc. SPIE, 10707, 1070710
Gutiérrez, C. P., Anderson, J. P., Hamuy, M., et al. 2014, ApJL, 786, L15
Gutiérrez, C. P., Anderson, J. P., Hamuy, M., et al. 2017, ApJ, 850, 89
Hamuy, M. 2003, ApJ, 582, 905
Harris, C. R., Millman, K. J., van der Walt, S. J., et al. 2020, Natur, 585, 357
Hiramatsu, D., Tsuna, D., Berger, E., et al. 2023, ApJL, 955, L8

Hosseinzadeh, G., Bostroem, K. A., & Gomez, S. 2023, Light Curve Fitting, v0.9.0, Zenodo, doi:10.5281/zenodo.8049154
Hosseinzadeh, G., Farah, J., Shrestha, M., et al. 2023, ApJL, 953, L16
Hosseinzadeh, G., & Gomez, S. 2020, Light Curve Fitting, v0.2.0, Zenodo, doi:10.5281/zenodo.4312178
Hosseinzadeh, G., Kilpatrick, C. D., Dong, Y., et al. 2022, ApJ, 935, 31
Hosseinzadeh, G., Valenti, S., McCully, C., et al. 2018, ApJ, 861, 63
Huang, F., Wang, X., Zampieri, L., et al. 2016, ApJ, 832, 139
Hunter, J. D. 2007, CSE, 9, 90
IRSA 2022, Galactic Dust Reddening and Extinction, doi:10.26131/IRSA537
Jacobson-Galán, W. V., Dessart, L., Jones, D. O., et al. 2022, ApJ, 924, 15
Jacobson-Galán, W. V., Dessart, L., Margutti, R., et al. 2023, ApJL, 954, L42
Kansky, J., Chilingarian, I., Fabricant, D., et al. 2019, PASP, 131, 075005
Katz, B., Sapir, N., & Waxman, E. 2012, ApJ, 747, 147
Kilpatrick, C. D., Izzo, L., Bentley, R. O., et al. 2023, MNRAS, 524, 2161
Koribalski, B. S., Staveley-Smith, L., Kilborn, V. A., et al. 2004, AJ, 128, 16
Kourkchi, E., Courtois, H. M., Graziani, R., et al. 2020, AJ, 159, 67
Kulkarni, S. R. 2020, arXiv:2004.03511
Levesque, E. M. 2017, Astrophysics of Red Supergiants (Bristol: IOP Publishing)
Li, L., Zhai, Q., Zhang, J., & Wang, X. 2023, TNSCR, 2023-241, 1
Li, W., Leaman, J., Chornock, R., et al. 2011, MNRAS, 412, 1441
Massey, P., Neugent, K. F., Ekström, S., Georgy, C., & Meynet, G. 2023, ApJ, 942, 69
McCully, C., Volgenau, N. H., Harbeck, D.-R., et al. 2018, Proc. SPIE, 10707, 107070K
McLeod, B., Fabricant, D., Nystrom, G., et al. 2012, PASP, 124, 1318
Morag, J., Sapir, N., & Waxman, E. 2023, MNRAS, 522, 2764
Morozova, V., Piro, A. L., & Valenti, S. 2017, ApJ, 838, 28
Morozova, V., Piro, A. L., & Valenti, S. 2018, ApJ, 858, 15
Munari, U., & Zwitter, T. 1997, A&A, 318, 269
Pearson, J., Hosseinzadeh, G., Sand, D. J., et al. 2023, ApJ, 945, 107
Piascik, A. S., Steele, I. A., Bates, S. D., et al. 2014, Proc. SPIE, 9147, 91478H
Poznanski, D., Prochaska, J. X., & Bloom, J. S. 2012, MNRAS, 426, 1465
Price-Whelan, A. M., Sipőcz, B. M., Günther, H. M., et al. 2018, AJ, 156, 123
Rabinak, I., & Waxman, E. 2011, ApJ, 728, 63
Reichart, D., Nysewander, M., Moran, J., et al. 2005, NCimC, 28, 767
Richmond, M. W., Treffers, R. R., Filippenko, A. V., et al. 1994, AJ, 107, 1022
Roth, K., Price, P., Gillies, K., Walker, S., & Miller, B. 2009, AAS Meeting Abstracts, 213, 476.10
Sand, D. J., Wyatt, S. D., Janzen, D., et al. 2023, TNSTR, 2023-223, 1
Sapir, N., Katz, B., & Waxman, E. 2011, ApJ, 742, 36
Sapir, N., Katz, B., & Waxman, E. 2013, ApJ, 774, 79
Sapir, N., & Waxman, E. 2017, ApJ, 838, 130
Schlafly, E. F., & Finkbeiner, D. P. 2011, ApJ, 737, 103
Shaya, E. J., Tully, R. B., Hoffman, Y., & Pomarède, D. 2017, ApJ, 850, 207
Smartt, S. J. 2015, PASA, 32, e016
Smith, M. P., Nordsieck, K. H., Burgh, E. B., et al. 2006, Proc. SPIE, 6269, 62692A
Smith, N. 2014, ARA&A, 52, 487
Smith, N., Li, W., Filippenko, A. V., & Chornock, R. 2011, MNRAS, 412, 1522
Soumagnac, M. T., Ganot, N., Irani, I., et al. 2020, ApJ, 902, 6
Spiro, S., Pastorello, A., Pumo, M. L., et al. 2014, MNRAS, 439, 2873
Tartaglia, L., Sand, D. J., Groh, J. H., et al. 2021, ApJ, 907, 52
Tartaglia, L., Sand, D. J., Valenti, S., et al. 2018, ApJ, 853, 62
Teja, R. S., Singh, A., Sahu, D. K., et al. 2022, ApJ, 930, 34
Terreran, G., Jacobson-Galán, W. V., Groh, J. H., et al. 2022, ApJ, 926, 20
Tody, D. 1986, Proc. SPIE, 627, 733
Tody, D. 1993, in ASP Conf. Ser. 52, Astronomical Data Analysis Software and Systems II, ed. R. J. Hanisch, R. J. V. Brissenden, & J. Barnes (San Francisco, CA: ASP), 173
Valenti, S., Benetti, S., Cappellaro, E., et al. 2008, MNRAS, 383, 1485
Valenti, S., Howell, D. A., Stritzinger, M. D., et al. 2016, MNRAS, 459, 3939
Valenti, S., Sand, D., Pastorello, A., et al. 2014, MNRAS, 438, 101
Van Dyk, S. D. 2017, RSPTA, 375, 20160277
Virtanen, P., Gommers, R., Oliphant, T. E., et al. 2020, NatMe, 17, 261
Wyatt, S., Shrestha, M., & Hosseinzadeh, G. 2023, PyMMT, v1.0.0, Zenodo, doi:10.5281/zenodo.8322354
Yaron, O., Perley, D. A., Gal-Yam, A., et al. 2017, NatPh, 13, 510
Young, D. 2022, Plot Results from ATLAS Force Photometry Service, https://gist.github.com/thespacedoctor/86777fa5a9567b7939e8d84fd8cf6a76